Crystal structure and Raman-active lattice vibrations of magnetic topological insulators $MnBi_2Te_4 \cdot n(Bi_2Te_3)$ ($n = 0, 1,...,6$)

I. R. Amiraslanov,[1,2,*] Z. S. Aliev,[2] P. A. Askerova,[1] E. H. Alizade,[1] Y. N. Aliyeva,[2,1] N. A. Abdullayev,[1,2] Z. A. Jahangirli,[1,2] M. M. Otrokov,[3,4] N. T. Mamedov,[1,2,†] and E. V. Chulkov[5,6,7]

[1]*Institute of Physics, Ministry of Science and Education, AZ1143 Baku, Azerbaijan*

[2]*Baku State University, AZ1148 Baku, Azerbaijan*

[3]*Centro de Fisica de Materiales (CFM-MPC), Centro Mixto CSIC-UPV/EHU, Donostia-San Sebastian, Basque Country, Spain*

[4]*IKERBASQUE, Basque Foundation for Science, Bilbao, Spain*

[5]*Departamento de Polímeros y Materiales Avanzados: Física, Química y Tecnología, Facultad de Ciencias Químicas, Universidad del País Vasco UPV/EHU, 20080 Donostia-San Sebastián, Basque Country, Spain*

[6]*Donostia International Physics Center (DIPC), 20018 Donostia-San Sebastian, Basque Country, Spain*

[7]*Saint Petersburg State University, Saint Petersburg 198504, Russia*

(Received 25 July 2022; revised 6 November 2022; accepted 9 November 2022; published 23 November 2022)

Further to the structure of the intrinsic magnetic topological insulators $MnBi_2Te_4 \cdot n(Bi_2Te_3)$ with $n < 4$, where index n is the number of quintuple Te-Bi-Te-Bi-Te building blocks inserted between the neighboring septuple Te-Bi-Te-Mn-Te-Bi-Te building blocks, the structure of the members with $n = 4$, 5, and 6 was studied using x-ray powder diffraction. The unit-cell parameters and atomic positions were obtained. The obtained and available structural data were summarized to show that the crystal structure of all members of $MnBi_2Te_4 \cdot n(Bi_2Te_3)$ follows the cubic close-packing principle, independently of the space group of the given member. Confocal Raman spectroscopy was then applied. Comparative analysis of the number, frequency, symmetry, and broadening of the vibration modes responsible for the lines in the Raman spectra of the systems with $n = 1, \ldots,6$, as well as $MnBi_2Te_4$ ($n = 0$) and Bi_2Te_3 ($n = \infty$) has shown that lattice dynamics of $MnBi_2Te_4 \cdot n(Bi_2Te_3)$ with $n > 0$ overwhelmingly dominates by the cooperative atomic displacements in the quintuple building blocks.

DOI: 10.1103/PhysRevB.106.184108

I. INTRODUCTION

The members of the tetradymite homological series $MnBi_2Te_4 \cdot n(Bi_2Te_3)$ are layered systems whose structure consists of quintuple Te-Bi-Te-Bi-Te (QL-) and septuple Te-Bi-Te-Mn-Te-Bi-Te (SL-) layer building blocks, separated by van der Waals (vdW) gaps [1]. These systems are currently considered as natural intrinsic magnetic topological heterostructures with index n indicating the number of nonmagnetic QLs inserted between the neighboring magnetic SLs [2]. Along with such prerequisites of nontrivial topology as strong spin-orbital interaction and inverted band gap [3–5], the distinctive feature of these quantum materials is a magnetic gap that appears within topological surface states, providing necessary conditions for the realization of quantum anomalous Hall state [6–8].

Although existence of the members with n up to 6 has been reported [2], in fact only the members with $n = 0$, 1, 2, and 3 have been studied in detail using various experimental and theoretical techniques [1,2,9–43]. In particular, available structure refinement and Raman-scattering studies [1,26–43] have been performed for systems with n less than 4, probably because of the obvious difficulties in the preparation of $MnBi_2Te_4 \cdot n(Bi_2Te_3)$ with high index n and unavailability of samples.

We have succeeded in this regard and present here the crystal structure of the members with $n = 4$, 5, and 6, summarize all available structural data for $MnBi_2Te_4 \cdot n(Bi_2Te_3)$, trace the evolution of Raman spectra of $MnBi_2Te_4 \cdot n(Bi_2Te_3)$ that embraces all n from 0 to 6 as well as $n = \infty$ (Bi_2Te_3), and provide a thorough analysis of the obtained Raman data.

II. SYNTHESIS AND CRYSTAL STRUCTURE OF $MnBi_2Te_4 \cdot n(Bi_2Te_3)$

A. Synthesis and crystal growth

Prior to the growth of the title compounds, the binaries MnTe and Bi_2Te_3 as precursors were synthesized from high-purity (99.999 wt. %) elemental manganese, bismuth, and tellurium purchased from Alfa Aesar. The synthesis of MnTe and Bi_2Te_3 was carried out in sealed quartz ampoules by melting the above elements at 1180 °C and 630 °C, respectively. To avoid the reaction of manganese with silica during melting, the inner wall of the ampoule was coated with graphite by the thermal decomposition of acetone. The polycrystalline $MnBi_2Te_4 \cdot n(Bi_2Te_3)$ compounds with different n were synthesized by comelting binaries in evacuated silica ampoules.

*iamiraslan@gmail.com

†n.mamedov.physics@bsu.edu.az

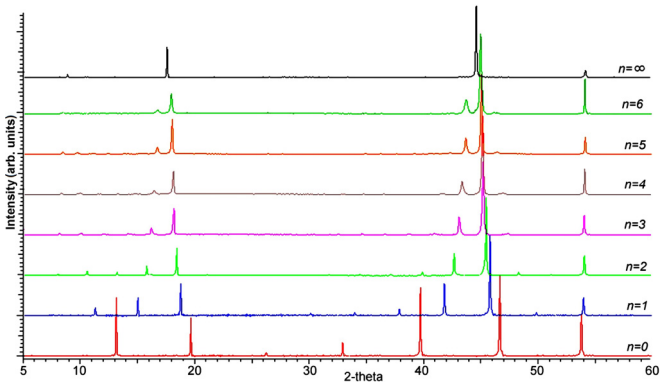

FIG. 1. The (0001) diffraction patterns of $MnBi_2Te_4 \cdot n(Bi_2Te_3)$ with different index n.

The temperature of synthesis was varied depending on the required n. For example, for $MnBi_2Te_4(n = 0)$ this temperature was 980 °C at which the melt was kept for 8 h, while $MnBi_4Te_7(n = 1)$ was synthesized at 900 °C, keeping the melt at this temperature for 8 h.

Since the primary crystallization of $MnBi_2Te_4 \cdot n(Bi_2Te_3)$ compounds (where $n = 0,1,2,3,4$) occur in narrow temperature ranges (less than 8 K) and they are adjacent to each other in the phase diagram, the growth of single-phase ingots is always a difficult task. The ingots of the $MnBi_2Te_4 \cdot n(Bi_2Te_3)$ compounds were grown from the melt using the vertical Bridgman-Stockbarger method [1]. The polycrystalline samples were placed in conical-bottom silica ampoules, which were sealed under a vacuum better than 10^{-4} Pa. The ampoules were kept in the high-temperature zone (T_1, $\sim$ 950 K) of the furnace for 12 h to complete the homogenization of the compositions. The ampoules moved from zone T_1 to zone T_2 (zone of low temperatures, $\sim$ 800 K) at a speed of 0.5 mm/h. The single-crystalline blocks of each compound were isolated from as-grown ingots using the employed x-ray diffraction (XRD) system.

B. X-ray diffraction characterization

X-ray diffraction (XRD) patterns were obtained using a Bruker XRD D2 Phaser (CuK_α; $5 \leqslant 2\theta \leqslant 100^\circ$) diffractometer. The Rietveld refinements of the crystal structures were performed using powder-diffraction data. The phase constitution analyses and structural refinements were performed using the EVA and TOPAS-4.2 software packages supplied together with the diffractometer.

The single-crystalline samples with an average size of $2 \times 2 \times 0.1\,mm^3$ were cleaved from the as-grown ingots of each homologous phase by the top-off procedure under an optical microscope. The (0001) XRD patterns of these samples are given in Fig. 1.

The space group and lattice parameters for each of the obtained members of the $MnBi_2Te_4 \cdot n(Bi_2Te_3)$ are given in Table I. Note that along with the data previously published [1,2] and reproduced here for structures with $n = \infty$, 0, 1, 2, and 3, this table also shows the data extracted in this work for $n = 4$, 5, and 6. The details regarding the extracted data are given in the next two subsections, together with the general building principle of $MnBi_2Te_4 \cdot n(Bi_2Te_3)$ structures.

C. Rietveld refinement of the crystal structure of $MnBi_{10}Te_{16}$ ($n = 4$)

Note that the atomic percent of manganese in $MnBi_2Te_4 \cdot n(Bi_2Te_3)$ is decreasing as $100/(5n + 7)$ with increasing n due to the stably increasing number of the Bi_2Te_3 QLs. Therefore, conduction of the conventional Rietveld refinement of the structures with large n requires sufficiently massive single crystals. While high-n tiny single crystals of a smaller volume can be successfully obtained from the as-grown ingots by cleaving and have already been used in reported XRD studies [1] and Raman studies presented in this work, the Rietveld refinement of the crystal structure for $n > 3$ has not been performed yet, because of the absence of enough massive single-phase crystalline samples.

In this work, we were unable to find a massive single-phase sample among the pieces detached from the as-grown nominally $n = 4$ ingot either. Nevertheless, a sample that contained a mixture of single-crystalline $n = 4$ (50.7%) and $n = 3$ (49.3%) phases and was suitable for structural analysis has been available.

Figure 2 displays the XRD pattern of this sample, together with Rietveld fitted pattern. A very good agreement between both patterns is observed. The space group and unit-cell

TABLE I. Space group and lattice parameters of $MnBi_2Te_4 \cdot n(Bi_2Te_3)$ with different n.

$MnBi_2Te_4 \cdot n(Bi_2Te_3)$				Unit-cell parameters		
Stoichiometric formula	Unit-cell content	n	Space group	a (Å)	c (Å)	QL (5) and SL (7) sequences
Bi_2Te_3	$Bi_2Te_3 \times 3$	∞	$R\text{-}3m$	4.386	30.497	−5−
$MnBi_2Te_4$	$MnBi_2Te_4 \times 3$	0	$R\text{-}3m$	4.3304(1)	40.956(2)	−7−
$MnBi_4Te_7$	$MnBi_4Te_7$	1	$P\text{-}3m1$	4.3601(1)	23.798(2)	−5−7−
$MnBi_6Te_{10}$	$MnBi_6Te_{10} \times 3$	2	$R\text{-}3m$	4.3685(2)	101.870(7)	−5−5 − 7−
$MnBi_8Te_{13}$	$MnBi_8Te_{13} \times 3$	3	$R\text{-}3m$	4.3927(8)	132.336(24)	−5−5 − 5−7−
$MnBi_{10}Te_{16}$	$MnBi_{10}Te_{16}$	4	$P\text{-}3m1$	4.3701(7)	54.304(9)	−5−5 − 5−5 − 7
$MnBi_{12}Te_{19}$[a]	$MnBi_{12}Te_{19} \times 3$	5	$R\text{-}3m$	4.370	193.50	−5−5 − 5−5 − 5−7−
$MnBi_{14}Te_{22}$[a]	$MnBi_{14}Te_{22} \times 3$	6	$R\text{-}3m$	4.370	223.89	−5−5 − 5−5 − 5−5 − 7−

[a]For structures with $n = 5$ and 6, parameter a is taken equal to that of the structure with $n = 4$, while parameter c is calculated from the diffraction patterns (Fig. 1, $n = 5,6$).

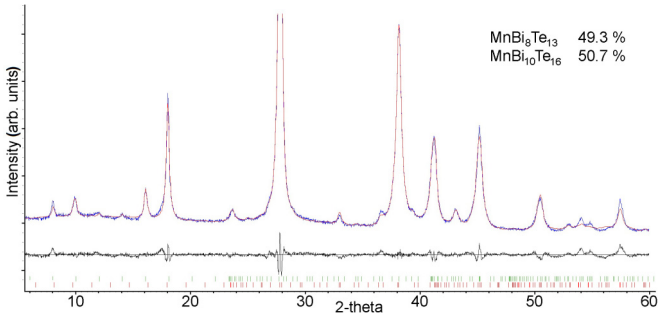

FIG. 2. XRD (blue curve) and Rietveld fitted (red curve) patterns of a crystalline mixture of 49.3% $MnBi_8Te_{13}$ and 50.7% $MnBi_{10}Te_{16}$. The difference curve is given beneath these patterns.

parameters obtained using Le Bail's refinement for $n = 4$ phase have been given earlier in Table I. Interatomic Mn-Te and Bi-Te distances are 2.98(3) and 2.94(4)–3.34(4) Å, respectively. Atomic positions refined up to $R_{\text{Bragg}} = 2.34\%$ are given in Supplemental Material, Table S1 [44], together with similar data for the other members of the $MnBi_2Te_4 \cdot n(Bi_2Te_3)$ homologous series.

D. Crystal structure of $MnBi_2Te_4 \cdot n(Bi_2Te_3)$ and cubic close-packing principle

In layered crystals, the stacking manner between the building blocks separated by vdW gaps usually varies leading to different polymorphs (polytypic forms) with cubic or hexagonal close packing or just to stacking faults in such polymorphs. A weak vdW bond provides favorable conditions for the above blocks to easily shift relative to each other overcoming small enough small-energy barriers between the various stable states. GaSe and MoS_2, which have many polymorphs [45,46], are just a few examples to mention among the vast number of layered crystals.

As a matter of fact, all $MnBi_2Te_4 \cdot n(Bi_2Te_3)$ structures are built up only according to the cubic close-packing rule (Fig. 3), even if the space group of the structure changes from R-3m for the members with $n = \infty$, 0, 2, and 3 to P-3m1 for $n = 1$ and 4 (Table I). The latter fact is illustrated by Fig. 3

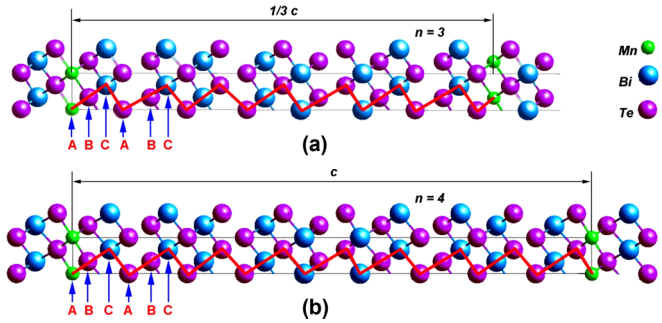

FIG. 3. Crystal structure of $MnBi_8Te_{13}$ with space group R-3m (a) and $MnB_{10}Te_{16}$ with space group P-3m1(b). A, B, and C indicate closely packed atoms with coordinates (0, 0), (1/3, 2/3), and (2/3, 1/3), respectively, in ***ab*** plane. The red zigzag line guides close (…ABC…) packing of Mn, Bi, and Te along the ***c*** direction.

with $n = 3$ (R-3m) and $n = 4$ (P-3m1) structures shown for comparison.

Thus, until now only the R-type rhombohedral unit cell is found for $MnBi_2Te_4 \cdot n(Bi_2Te_3)$ with $n = \infty$, 0, 2, and 3, while the P-type trigonal or hexagonal polymorphs are absent. On the other hand, the R-type polymorph is not found for $n = 1$ and $n = 4$ members of the $MnBi_2Te_4 \cdot n(Bi_2Te_3)$ family which crystallize into a trigonal structure with primitive (P-type) unit cell. Extending this rule to higher$-n$ members, it is easy to predict their structures and space groups. The latter can be only P-3m1 if one-third of the number of atoms in a chemical formula is an integer or R-3m in the rest cases. Moreover, following this rule and using the already accurately known structural data of SLs and QLs from which each $MnBi_2Te_4 \cdot n(Bi_2Te_3)$ structure is built up, it is not difficult to calculate the lattice parameters and atomic positions for arbitrary n. It is exactly in this way the structure of the members with $n = 5$ and $n = 6$ has been described after a comparison of the calculated data with the results of the XRD examination. Tables S1 and S2 [44] provide atomic coordinates for all $MnBi_2Te_4 \cdot n(Bi_2Te_3)$ studied in this work.

III. RAMAN SPECTRA OF $MnBi_2Te_4 \cdot n(Bi_2Te_3)$

A. Experimental technique

Raman scattering of $MnBi_2Te_4 \cdot n(Bi_2Te_3)$ was studied with the aid of a confocal microspectrometer Nanofinder 30 (Tokyo Instr., Japan). Second harmonic (532 nm) of Nd:yttrium-aluminum-garnet laser with a maximum output power of 10 mW was used as excitation source, and the cross-sectional beam diameter was 4 μm. Diffraction grating with 1800 grooves per mm provided a spectral resolution of 0.5 cm^{-1}. The spectra were detected using a photon-counting charge-coupled device camera cooled down to −100 °C; the exposure time was usually 1 min. The Raman signal was filtered out using edge filters LP03-532RU-50 (Semrock Company). The Raman spectra were taken in backscattering geometry at room temperature.

B. Raman-active modes of $MnBi_2Te_4 \cdot n(Bi_2Te_3)$

According to the performed site-symmetry analysis based on the structural data in Tables S1 and S2 [44], the number of vibration modes active in Raman scattering of $MnBi_2Te_4 \cdot n(Bi_2Te_3)$ has to grow with rising n from 0 to 6 (Table II, third row), because of the growth of the number of atoms in the elementary cell.

As shown in Fig. 4 with normalized experimental spectra (black lines) and deconvoluted spectra (green lines) of $MnBi_2Te_4 \cdot n(Bi_2Te_3)$, in fact, the number of these modes is not following the above expectation. While the number of lines in Raman spectra of the terminate members, $MnBi_2Te_4(n = 0)$ and Bi_2Te_3 ($n = \infty$) corresponds to the number of lines given by the site-symmetry analysis for bulk crystals, this number for the rest of the $MnBi_2Te_4 \cdot n(Bi_2Te_3)$ members is constant and equals 4, independently of n. value. Not shown in Fig. 4, the mode E_g^1 of $MnBi_2Te_4(n = 0)$ has been experimentally detected in a couple of recent works [38,40], making the total number of the observed lines in the Raman spectrum equal to 6. Disappearance of the mode E_g^1

TABLE II. The number (N) of atoms in the unit cell (third row), the number of modes of A_{1g} and E_g symmetry (fourth row), and the total number of modes (fifth row) for each member of $MnBi_2Te_4 \cdot n(Bi_2Te_3)$. E_g mode is doubly degenerate

Compound	Bi_2Te_3	$MnBi_2Te_4$	$MnBi_4Te_7$	$MnBi_6Te_{10}$	$MnBi_8Te_{13}$	$MnBi_{10}Te_{16}$	$MnB_{12}Te_{19}$	$MnBi_{14}Te_{22}$
n	∞	0	1	2	3	4	5	6
N	5	7	12	17	22	27	32	37
Modes	$2A_{1g} + 2E_g$	$3A_{1g} + 3E_g$	$6A_{1g} + 6E_g$	$8A_{1g} + 8E_g$	$11A_{1g} + 11E_g$	$13A_{1g} + 13E_g$	$16A_{1g} + 16E_g$	$18A_{1g} + 18E_g$
Number	4	6	12	16	22	26	32	36

from Raman spectra of $MnBi_2Te_4 \cdot n(Bi_2Te_3)$ with $n = 5$, 6, and ∞ in Fig. 4 is caused by instrumental limitations and the total number (4) of lines is preserved.

For example, $MnBi_4Te_7(n = 1)$ shows only 4 (Fig. 4) out of the expected 12 modes (Table II). For the rest of the members of $MnBi_2Te_4 \cdot n(Bi_2Te_3)$ with $1 < n < \infty$ the difference between the expected and real number of lines is even more essential by comparison.

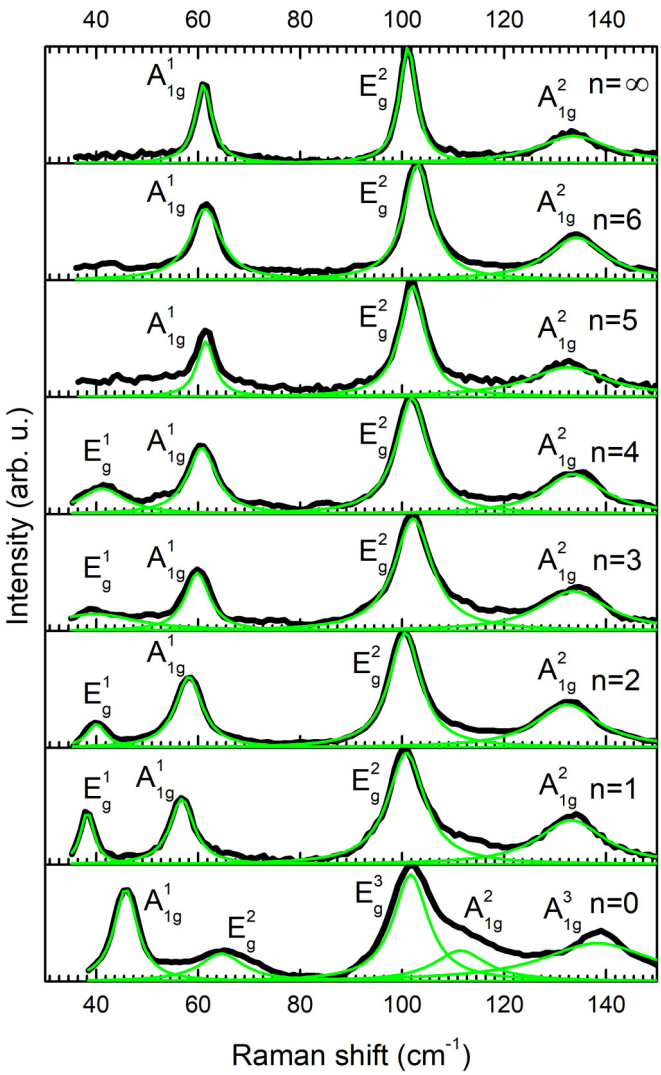

FIG. 4. Normalized Raman spectra (black lines) of $MnBi_2Te_4 \cdot n(Bi_2Te_3)$ for $n = 0$, 1, 2, 3, 4, 5, 6, and ∞. Results of deconvolution are shown by green lines.

The linewidth given in Table III for each mode observed in Raman spectra in Fig. 4 witnesses the absence of any broadening of the Raman lines. Such broadening would have manifested itself if the number of the Raman lines were increasing with rising n. In other words, Raman modes in Fig. 4 are the only normal vibrations active in Raman scattering of $MnBi_2Te_4 \cdot n(Bi_2Te_3)$.

For $MnBi_2Te_4(n = 0)$ that was studied thoroughly [1,30,36–41] and consists only of SLs, symmetry notations of vibration modes in Fig. 4 coincide with those of recent work [38] where these symmetries were confirmed by the measurements of the polarization of the modes. Starting from $MnBi_4Te_7(n = 1)$, for all members containing both SLs and QLs, and for Bi_2Te_3 ($n = \infty$), the symmetry of each mode in Fig. 4 follows the theoretical work [45] that considered Raman-active modes of free-standing QLs of Bi_2Te_3. The reason for this is a very close correspondence between the results calculated for the n number of QLs of Bi_2Te_3 and obtained for $MnBi_2Te_4 \cdot n(Bi_2Te_3)$ with the same index n. Such correspondence becomes obvious after the careful comparison of the obtained Raman data and the available results for Bi_2Te_3.

C. Lattice dynamics of $MnBi_2Te_4 \cdot n(Bi_2Te_3)$ and Bi_2Te_3

The frequency behavior of the Raman-active modes with changing n in $MnBi_2Te_4 \cdot n(Bi_2Te_3)$ is shown in Fig. 5.

The most noticeable frequency change occurs within the first two members of $MnBi_2Te_4 \cdot n(Bi_2Te_3)$ with $n = 0$ and $n = 1$. As seen from Fig. 5, except for those of E^2_g and E^3_g, the frequencies of the modes with the same symmetry in $MnBi_2Te_4$ and $MnBi_4Te_7$ noticeably differ from each other

TABLE III. Full width at half maximum (FWHM) of the Raman lines of the vibration modes of $MnBi_2Te_4 \cdot n(Bi_2Te_3)$ with different n.

	FWHM (cm^{-1})					
n	E^1_g	E^2_g	E^3_g	A^1_{1g}	A^2_{1g}	A^3_{1g}
0		10.5	8.3	5.54	12.6	26.6
1	3.2	8.7		5.7	15.8	
2	4.5	7.5		6.4	15.2	
3	21	8.9		5.8	16.5	
4	10	7.6		6.8	14.4	
5		6.1		4.2	19.1	
6		6.7		7.4	13.9	
∞		4		4.0	17.4	

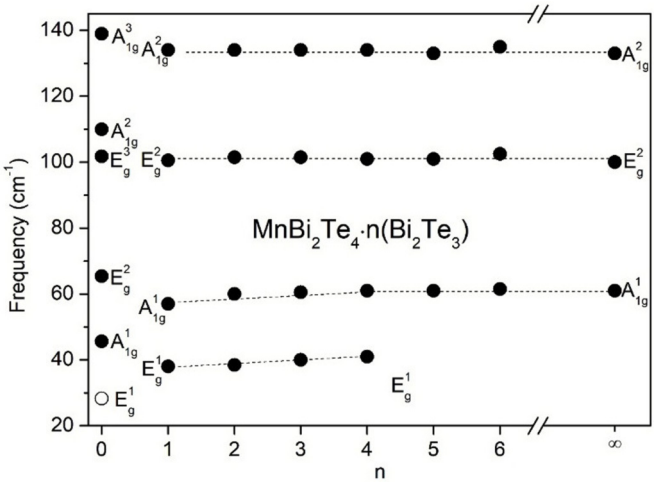

FIG. 5. Dependence of the frequency of the modes observed in the Raman spectra on the number (n) of QLs inserted between SLs in $MnBi_2Te_4 \cdot n(Bi_2Te_3)$. Dashed lines connect the frequencies of the modes with similar displacement fields. The open circle in Fig. 5 indicates the reported value [38,40,41] of the frequency of E_g^1 mode of $MnBi_2Te_4 (n = 0)$. The modes with the same symmetry for $n = 0$ ($MnBi_2Te_4$) and $n = 1$ ($MnBi_4Te_7$) are not connected because of the different displacement fields, as explained in the text.

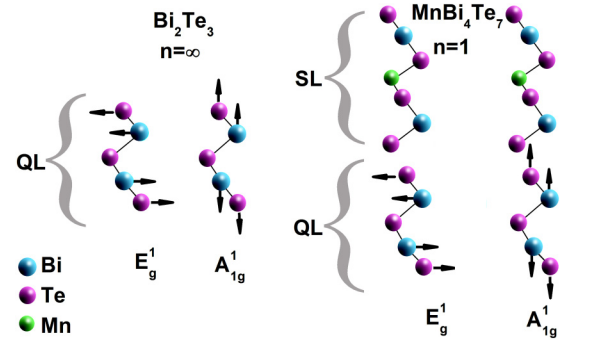

FIG. 6. Left: Displacement fields of the low-frequency Raman active modes E_g^1 and A_{1g}^1 of Bi_2Te_3 ($n = \infty$). Right: Displacement fields of E_g^1 and A_{1g}^1 Raman-active modes of $MnBi_4Te_7$ ($n = 1$), right figure. Arrows indicate only the direction of the displacements occurring parallel (horizontal arrows) and perpendicular (vertical arrows) to the layer plane for E_g^1- and A_{1g}^1-type vibrations, respectively.

in a similar frequency range. (Note that in spite of the same symmetry the displacement fields of the modes are different.) In Fig. 5 the open circle indicates the reported value [38,40,41] of the frequency of E_g^1 mode of $MnBi_2Te_4 (n = 0)$. This mode corresponds to the in-plane in-phase displacements of Bi and Te in SLs. The other in-plane in-phase mode of $MnBi_2Te_4$ is A_{1g}^1. The frequencies of the in-plane in-phase counterparts of these modes in $MnBi_4Te_7$ ($n = 1$) are appreciably higher and obey the relation $\omega_{n=1}/\omega_{n=0} \approx [(2m_{Te} + m_{Bi})/(m_{Te} + m_{Bi})]^{1/2}$, where m_{Te} and m_{Bi} are the atomic masses of Te and Bi. It is then suggestive to ascribe the low-frequency modes of $MnBi_4Te_7$, E_g^1 and A_{1g}^1, to the displacements of Te and Bi in QLs of Bi_2Te_3 rather than SLs like in the case of $MnBi_2Te_4$. Contrary to the expectations, the number of the modes observed after the insertion of just 1 QL of Bi_2Te_3 between SLs of $MnBi_2Te_4$ to form $MnBi_4Te_7$ is not increasing but is down to the number of the modes observed for Bi_2Te_3 (Table II). Importantly enough, the number of modes and their symmetry for 1 and more QLs of Bi_2Te_3 and bulk Bi_2Te_3 is the same and the low-frequency modes of 1 QL of Bi_2Te_3 are redshifted in comparison with their bulk counterparts [45]. According to Fig. 5, quite similar dispersion is observed for the low-frequency E_g^1 and A_{1g}^1 modes in structures with $n > 0$.

In other words, there has to be a one-to-one correspondence between our results for structures with $n = 1$, 2, 3, 4, 5, and 6 and those for 1, 2, 3, 4, 5, and 6 QLs of Bi_2Te_3. In fact, our results practically coincide with the results obtained by Zhao *et al.* [46] for 2–11 QLs of Bi_2Te_3 on SiO_2/Si substrate. According to the latter results, the low-frequency E_g^1 appeared only for 2 QLs of Bi_2Te_3 and was no longer observed for the greater number of QLs, which corroborates the dying intensity of this mode with increasing index n in our case. Another coincidence is the blueshift of A_{1g}^1 mode with raising the number of QLs from 2 to 4, as well as the fixed frequency of this mode for larger number of QLs [46].

The above described drives us to a conclusion that the displacement fields of the low-frequency lattice modes of $MnBi_2Te_4 \cdot n(Bi_2Te_3)$ with $n = 1$ ($MnBi_4Te_7$) are as shown on the right in Fig. 6, where displacement fields of these modes in Bi_2Te_3 are also given on the left for comparison.

The high-frequency antiphase out-of-plane modes, E_g^2 and A_{1g}^2 for $n > 0$ in Fig. 5, are difficult to attribute to QLs or SLs or to both simultaneously. The frequencies of E_g^2 modes of $MnBi_2Te_4$ and the rest of the members of $MnBi_2Te_4 \cdot n(Bi_2Te_3)$ are identical and the modes are indistinguishable from one another. The A_{1g}^2 mode of $MnBi_2Te_4$ no longer exists for $n > 0$ and the closest to the A_{1g}^2 mode of the structures with $n > 0$ is the A_{1g}^3 mode of $MnBi_2Te_4$ (Fig. 5). Although there is a small (2%) frequency difference between A_{1g}^3 mode of the structure with $n = 0$ and A_{1g}^2 mode of the structures with $n > 0$, change, this is not enough to attribute A_{1g}^2 mode to QLs. Decisive in this regard (it concerns the E_g^2 mode, too) is the fact that participation of QLs in low-frequency vibrations dictates participation of QLs in high-frequency vibrations, too. Such assignment is strongly supported by the limited fixed-to-four number of the Raman lines observed for $MnBi_2Te_4 \cdot n(Bi_2Te_3)$ with $n > 0$.

As seen in Fig. 7, while the share of QLs in the scattering volume increases, the share of SLs decreases, reaching only 14%. However, even this not-large share (not speaking of 50% for $n = 1$) is quite enough to detect Raman modes of SLs by such a sensitive technique as confocal Raman spectroscopy, if such modes would have existed and manifested themselves like in the case of even 1 SL of $MnBi_2Te_4$ [38,40].

Thus, Raman-active part of lattice dynamics of $MnBi_2Te_4 \cdot n(Bi_2Te_3)$ with n in the range $1 \leqslant n \leqslant \infty$ is determined by lattice dynamics of nQLs of Bi_2Te_3. Note that this is not too surprising since such dynamics are a prerequisite of the limiting case of Bi_2Te_3.

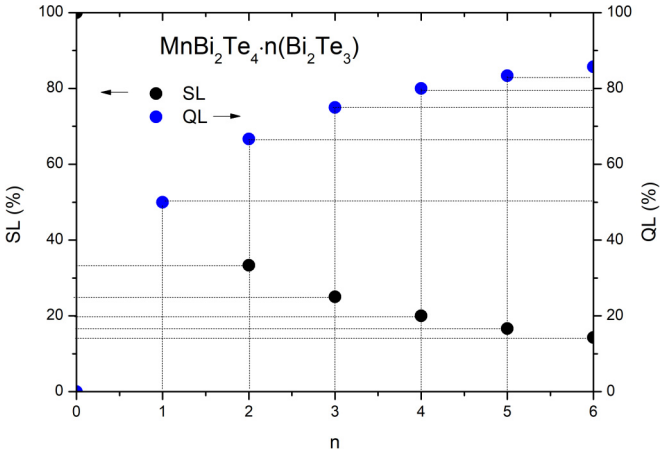

FIG. 7. Percentage of SLs (left scale, black solid circles) and QLs (right scale, blue solid circles) in $MnBi_2Te_4 \cdot n(Bi_2Te_3)$, taken as $100\%/(n+1)$ and $100\%\ n/(n+1)$ for SLs and QLs, respectively.

IV. SUMMARY

$MnBi_2Te_4 \cdot n(Bi_2Te_3)$ single crystals with integer index n running from 0 to 6 have been successfully grown and characterized by x-ray powder diffraction and confocal Raman spectroscopy.

The crystal structure has been established for the system with $n = 4$ by Rietveld refinement and calculated for the systems with $n = 4$ and 5 by using the cubic close-packing rule and their XRD patterns. This principle is shown to underlie the crystal structure arrangement of each member of $MnBi_2Te_4 \cdot n(Bi_2Te_3)$, accounts for the absence of polymorphs, and permits only *R*-3*m* or *P*-3*m*1 space group of the members of this homological series. Atomic positions, space groups, and lattice parameters are summarized for all available $MnBi_2Te_4 \cdot n(Bi_2Te_3)$ to provide a database demanded for theoretical calculations.

Raman spectra, earlier available only for the systems with index $n < 4$, have been obtained for systems with $n = 4$, 5, and 6. Essential disagreement between the results of site-symmetry analysis and experimental observations regarding the number of the vibration modes active in Raman scattering of $MnBi_2Te_4 \cdot n(Bi_2Te_3)$ with index n in the range $1 \leqslant n \leqslant \infty$ has been found. This disagreement can be lifted off if the lattice dynamics of $MnBi_2Te_4 \cdot n(Bi_2Te_3)$ with given index n and that of nQLs of Bi_2Te_3 are similar. The only difference between the $MnBi_2Te_4 \cdot n(Bi_2Te_3)$ and Bi_2Te_3 is that displacement field of each mode in the former includes atomic displacements in QLs and infinitesimally small atomic displacements in SLs, while only atomic displacements in QLs form lattice modes in the latter.

Magnetic Mn atoms do not participate in displacement fields of the modes active in Raman scattering but contribute in IR-active modes. Unfortunately, the reported infrared studies [24,47,48] were focused on the coupling between magnetic ordering and electronic structure rather than infrared active phonons that are yet to be studied for $MnBi_2Te_4 \cdot n(Bi_2Te_3)$. Besides, $MnBi_2Te_4 \cdot n(Bi_2Te_3)$ systems with high index n are of special interest, because of the crossover between the 3D ($n = 3$ [49]) and 2D ferromagnetic cases. The system with $n = 4$ is bordering these cases while systems with $n = 5$ and 6 are very likely to have truly magnetically decoupled SLs, bringing about conditions for the realization of quantum anomalous Hall state.

ACKNOWLEDGMENTS

This work was performed within the research program "Development of preparation technology of multifunctional convertors based on nanosized structures" and was supported by TÜBİTAK - ANAS Project No. 120N296. M.M.O. acknowledges the support by Spanish Ministerio de Ciencia e Innovación (Grant No. PID2019-103910GB-100). E.V.C. acknowledges support from Saint Petersburg State University (Project ID No. 90383050).

[1] Z. S. Aliev, I. R. Amiraslanov, D. I. Nasonova, A. V. Shevelkov, N. A. Abdullayev, Z. A. Jahangirli, E. N. Orujlu, M. M. Otrokov, N. T. Mamedov, M. B. Babanly, and E. V. Chulkov, Novel ternary layered manganese bismuth tellurides of the MnTe-Bi_2Te_3 system: Synthesis and crystal structure, J. Alloys Compd. **789**, 443 (2019).

[2] I. I. Klimovskikh, M. M. Otrokov, D. Estyunin, S. V. Eremeev, S. O. Filnov, A. Koroleva, E. Shevchenko, V. Voroshnin, I. P. Rusinov, M. Blanco-Rey *et al.*, Tunable 3D/2D magnetism in the $(MnBi_2Te_4)(Bi_2Te_3)_m$ topological insulators family, npj Quantum Mater. **5**, 54 (2020).

[3] M. Z. Hasan and C. L. Kane, Colloquium: Topological insulators, Rev. Mod. Phys. **82**, 3045 (2010).

[4] S. V. Eremeev, G. Landolt, T. V. Menshchikova, B. Slomski, Y. M. Koroteev, Z. S. Aliev, M. B. Babanly, J. Henk, A. Ernst, L. Patthey, A. Eich, A. A. Khajetoorians, J. Hagemeister, O. Pietzsch, J. Wiebe, R. Wiesendanger, P. M. Echenique, S. S. Tsirkin, I. R. Amiraslanov, J. H. Dil, and E. V. Chulkov, Atom-specific spin mapping and buried topological states in a homologous series of topological insulators, Nat. Commun. **3**, 635 (2012).

[5] S. V. Eremeev, Y. M. Koroteev, and E. V. Chulkov, Effect of the atomic composition of the surface on the electron surface states in topological insulators $A_2^{\mathrm{V}} B_3^{\mathrm{VI}}$, JETP Lett. **91**, 387 (2010).

[6] C.-Z. Chang, J. Zhang, X. Feng, J. Shen, Z. Zhang, M. Guo, K. Li, Y. Ou, P. Wei, L. Wang, Z.-Q. Ji, Y. Feng, S. Ji, X. Chen, J. Jia, X. Dai, Z. Fang, S.-C. Zhang, K. He, Y. Wang, L. Lu, X.-C. Ma, and Q.-K. Xue, Experimental observation of the quantum anomalous Hall effect in a magnetic topological insulator, Science **340**, 167 (2013).

[7] M. M. Otrokov, T. V. Menshchikova, M. G. Vergniory, I. P. Rusinov, A. Yu. Vyazovskaya, Yu. M. Koroteev, G. Bihlmayer, A. Ernst, P. M. Echenique, A. Arnau, and E. V. Chulkov, Highly-ordered wide bandgap materials for quantized

anomalous Hall and magnetoelectric effects, 2D Mater. **4**, 025082 (2017).

[8] M. M. Otrokov, I. I. Klimovskikh, H. Bentmann, D. Estyunin, A. Zeugner, Z. S. Aliev, S. Gaß, A. U. B. Wolter, A. V. Koroleva, A. M. Shikin *et al.*, Prediction and observation of an antiferromagnetic topological insulator**,** Nature (London) **576**, 416 (2019).

[9] P. Rani, A. Saxena, R. Sultana, V. Nagpal, S. Islam, S. Patnaik, and V. P. S. Awana, Crystal growth and basic transport and magnetic properties of $MnBi_2Te_4$, J. Supercond. Nov. Magn. **32**, 3705 (2019).

[10] J. Wu, F. Liu, M. Sasase, K. Ienaga, Y. Obata, R. Yukawa, K. Horiba, H. Kumigashira, S. Okuma, T. Inoshita, and H. Hosono, Natural van der Waals heterostructural single crystals with both magnetic and topological properties, Sci. Adv. **5**, eaax9989/1 (2019).

[11] J. Ge, Y. Liu, J. Li, H. Li, T. Luo, Y. Wu, Y. Xu, and J. Wang, High-Chern-number and high-temperature quantum Hall effect without Landau levels, Natl. Sci. Rev. **7**, 1280 (2020).

[12] J. Li, Y. Li, S. Du, Z. Wang, B.-L. Gu, S.-C. Zhang, K. He, W. Duan, and Y. Xu, Intrinsic magnetic topological insulators in van der Waals layered $MnBi_2Te_4$-family materials, Sci. Adv. **5**, eaaw5685 (2019).

[13] M. Z. Shi, B. Lei, C. S. Zhu, D. H. Ma, J. H. Cui, Z. L. Sun, J. J. Ying, and X. H. Chen, Magnetic and transport properties in the magnetic topological insulators $MnBi_2Te_4 \cdot (Bi_2Te_3)n$ $(n = 1, 2)$, Phys. Rev. B **100**, 155144 (2019).

[14] S. Tian, S. Gao, S. Nie, Y. Qian, C. Gong, Y. Fu, H. Li, W. Fan, P. Zhang, T. Kondo, S. Shin, J. Adell, H. Fedderwitz, H. Ding, Z. Wang, T. Qian, and H. Lei, Magnetic topological insulator $MnBi_6Te_{10}$ with a zero-field ferromagnetic state and gapped Dirac surface states, Phys. Rev. B **102**, 035144 (2020).

[15] R. C. Vidal, A. Zeugner, J. I. Facio, R. Ray, M. H. Haghighi, A. U. B. Wolter, L. T. C. Bohorquez, F. Caglieris, S. Moser, T. Figgemeier, T. R. F. Peixoto *et al.*, Topological Electronic Structure and Intrinsic Magnetization in $MnBi_4Te_7$: A Bi_2Te_3 Derivative with a Periodic Mn Sublattice, Phys. Rev. X **9**, 041065 (2019).

[16] C. Hu, L. Ding, K. N. Gordon, B. Ghosh, H. Li, S.-W. Lian, A. G. Linn, H.-J. Tien, C.-Y. Huang, P. V. S. Reddy, B. Singh, A. Agarwal, A. Bansil, S.-Y. Xu, H. Lin, H. Cao, T.-R. Chang, D. Dessau, and N. Ni, Realization of an intrinsic ferromagnetic topological state in $MnBi_8Te_{13}$, Sci. Adv. **6**, eaba4275 (2020).

[17] B. Chen, F. Fei, D. Zhang, B. Zhang, W. Liu, S. Zhang, P. Wang, B. Wei, Y. Zhang, Z. Zuo *et al.*, Intrinsic magnetic topological insulator phases in the Sb doped $MnBi_2Te_4$ bulks and thin flakes, Nat. Commun. **10**, 4469 (2019).

[18] M. Garnica, M. M. Otrokov, P. C. Aguilar, I. I. Klimovskikh, D. Estyunin, Z. S. Aliev, I. R. Amiraslanov, N. A. Abdullayev, V. N. Zverev, M. B. Babanly, N. T. Mamedov, A. M. Shikin, A. Arnau, A. L. Vázquez de Parga, E. V. Chulkov, and R. Miranda, Native point defects and their implications for the Dirac point gap at $MnBi_2Te_4(0001)$, npj Quantum Mater. **7**, 7 (2022).

[19] J.-Q. Yan, Y. H. Liu, D. Parker, Y. Wu, A. A. Acze, M. Matsuda, M. A. McGuire, and B. C. Sales, A-type antiferromagnetic order in $MnBi_4Te_7$ and $MnBi_6Te_{10}$ single crystals, Phys. Rev. Mater **4**, 054202 (2020).

[20] P.-F. Zhu, X.-G. Ye, J.-Z. Fang, P.-Z. Xiang, R.-R. Li, D.-Y. Xu, Z. Wei, J.-W. Mei, S. Liu, D.-P. Yu, and Z.-M. Liao, From negative to positive magnetoresistance in the intrinsic magnetic topological insulator $MnBi_2Te_4$, Phys. Rev. B **101**, 075425 (2020).

[21] A. Tan, V. Labracherie, N. Kunchur, A. U. B. Wolter, J. Cornejo, J. Dufouleur, B. Büchner, A. Isaeva, and R. Giraud, Metamagnetism of Weakly Coupled Antiferromagnetic Topological Insulators, Phys. Rev. Lett. **124**, 197201 (2020).

[22] Y. Deng, Y. Yu, M. Z. Shi, Z. Guo, Z. Xu, J. Wang, X. H. Chen, and Y. Zhang, Quantum anomalous Hall effect in intrinsic magnetic topological insulator $MnBi_2Te_4$, Science **367**, 895 (2020).

[23] C. Liu, Y. Wang, H. Li, Y. Wu, Y. Li, J. Li, K. He, Y. Xu, J. Zhang, and Y. Wang, Robust axion insulator and Chern insulator phases in a two-dimensional antiferromagnetic topological insulator, Nat. Mater. **19**, 522 (2020).

[24] B. Xu, Y. Zhang, E. H. Alizade, Z. A. Jahangirli, F. Lyzwa, E. Sheveleva, P. Marsik, Y. K. Li, Y. G. Yao, Z. W. Wang, B. Shen, Y. M. Dai, V. Kataev, M. M. Otrokov, E. V. Chulkov, N. T. Mamedov, and C. Bernhard, Infrared study of the multiband low-energy excitations of the topological antiferromagnet $MnBi_2Te_4$, Phys. Rev. B **103**, L121103 (2021).

[25] J. Wu, F. Liu, C. Liu, Y. Wang, C. Li, Y. Lu, S. Matsuishi, and H. Hosono, Toward 2D magnets in the $(MnBi_2Te_4)$ $(Bi_2Te_3)_n$ bulk crystal**,** Adv. Mater. **32**, 2001815 (2020).

[26] H. Li, Sh. Liu, C. Liu, J. Zhang, Y. Xu, R. Yu, Y. Wu, Y. Zhang, and Sh. Fan, Antiferromagnetic topological insulator $MnBi_2Te_4$: Synthesis and magnetic properties, Phys. Chem. Chem. Phys. **22**, 556 (2020).

[27] A. Zeugner, F. Nietschke, A. U. B. Wolter, S. Gaß, R. C. Vidal, T. R. F. Peixoto, D. Pohl, C. Damm, A. Lubk, R. Hentrich, S. K. Moser, C. Fornari, C. H. Min, S. Schatz, K. Kißner, M. Ünzelmann, M. Kaiser, F. Scaravaggi, B. Rellinghaus, K. Nielsch, C. Hess, B. Büchner, F. Reinert, H. Bentmann, O. Oeckler, T. Doert, M. Ruck, and A. Isaeva, Chemical aspects of the candidate antiferromagnetic topological insulator $MnBi_2Te_4$, Chem. Mater. **31**, 2795 (2019).

[28] J.-Q. Yan, Z. Huang. W. Wu, and A. F. May, Vapor transport growth of $MnBi_2Te_4$ and related compounds, J. Alloys Compd. **906**, 164327 (2022).

[29] J.-Q. Yan, Q. Zhang, T. Heitmann, Z. Huang, K. Y. Chen, J.-G. Cheng, W. Wu, D. Vaknin, B. C. Sales, and R. J. McQueeney, Crystal growth and magnetic structure of $MnBi_2Te_4$, Phys. Rev. Mater. **3**, 064202 (2019).

[30] L. Ding, Ch. Hu, F. Ye, E. Feng, N. Ni, and H. Cao, Crystal and magnetic structures of magnetic topological insulators $MnBi_2Te_4$ and $MnBi_4Te_7$, Phys. Rev. B **101**, 020412(R) (2020).

[31] S. Roychowdhury, S. Singh, S. N. Guin, N. Kumar, T. Chakraborty, W. Schnelle, H. Borrmann, Ch. Shekhar, and C. Felser, Giant topological Hall effect in the noncollinear phase of two-dimensional antiferromagnetic topological insulator $MnBi_4Te_7$, Chem. Mater. **33**, 8343 (2021).

[32] A. Gao, Y.-F. Liu, C. Hu, J.-X. Qiu, C. Tzschaschel, B. Ghosh, S.-C. Ho, D. Bérubé, R. Chen, H. Sun *et al.*, Layer Hall effect in a 2D topological axion antiferromagnet, Nature (London) **595**, 521 (2021).

[33] A. M. Shikin, D. A. Estyunin, I. I. Klimovskikh, S. O. Filnov, E. F. Schwier, S. Kumar, K. Miyamoto, T. Okuda, A. Kimura, K. Kuroda, K. Yaji, S. Shin, Y. Takeda, Y. Saitoh, Z. S. Aliev, N. T. Mamedov, I. R. Amiraslanov, M. B. Babanly, M. M. Otrokov, S. V. Eremeev, and E. V. Chulkov, Nature of the Dirac gap modulation and surface magnetic interaction in axion

antiferromagnetic topological insulator $MnBi_2Te_4$, Sci. Rep. **10**, 13226 (2020).

[34] R. Lu, H. Sun, S. Kumar, Y. Wang, M. Gu, M. Zeng, Y.-J. Hao, J. Li, J. Shao, X.-M. Ma, Z. Hao, K. Zhang, W. Mansuer, J. Mei, Y. Zhao, C. Liu, K. Deng, W. Huang, B. Shen, K. Shimada, E. F. Schwier, C. Liu, Q. Liu, and C. Chen, Half-magnetic Topological Insulator with Magnetization-Induced Dirac Gap at a Selected Surface, Phys. Rev. X **11**, 029902(E) (2021).

[35] A. M. Shikin, D. A. Estyunin, N. L. Zaitsev, D. Glazkova, I. I. Klimovskikh, S. O. Filnov, A. G. Rybkin, E. F. Schwier, S. Kumar, A. Kimura, N. T. Mamedov, Z. S. Aliev, M. B. Babanly, K. Kokh, O. E. Tereshchenko, M. M. Otrokov, E. V. Chulkov, K. A. Zvezdin, and A. K. Zvezdin, Sample-dependent Dirac-point gap in $MnBi_2Te_4$ and its response to applied surface charge: A combined photoemission and *ab initio* study, Phys. Rev. B **104**, 115168 (2021).

[36] M. Rodriguez-Vega, A. Leonardo, and G. A. Fiete, Group theory study of the vibrational modes and magnetic order in the topological antiferromagnet $MnBi_2Te_4$, Phys. Rev. B **102**, 104102 (2020).

[37] C. Pei, Y. Xia, J. Wu, Y. Zhao, L. Gao, T. Ying, B. Gao, N. Li, W. Yang, D. Zhang, H. Gou, Y. Chen, H. Hosono, G. Li, and Qi Y, Pressure-induced topological and structural phase transitions in an antiferromagnetic topological insulator, Chin. Phys. Lett. **37**, 066401 (2020).

[38] J. Choe, D. Lujan, M. Rodriguez-Vega, Z. Ye, A. Leonardo, J. Quan, T. N. Nunley, L-J. Chang, S.-F. Lee, J. Yan, G. A. Fiete, R. He, and X. Li, Electron-phonon and spin-lattice coupling in atomically thin layers of $MnBi_2Te_4$, Nano Lett. **21**, 6139 (2021).

[39] Yu. Cho, J. H. Kang, L. Liang, M. Taylor, X. Kong, S. Ghosh, F. Kargar, Ch. Hu, A. A. Balandin, A. A. Puretzky, N. Ni, and Ch. W. Wong, Phonon modes and Raman signatures of $MnBi_{2n}$ Te_{3n+1} ($n = 1,2,3,4$) magnetic topological heterostructures, Phys. Rev. Res. **4**, 013108 (2022).

[40] G. Li, X. Wu, Y. Gao, X. Ma, F. Hou, H. Cheng, Q. Huang, Y.-Ch. Wu, M. C. DeCapua, Y. Zhang, J. Lin, Ch. Liu, L. Huang, Y. Zhao, J. Yan, and M. Huang, Observation of ultra-strong coupling between substrate and the magnetic topological insulator $MnBi_2Te_4$, Nano Lett. **22**, 3856 (2022).

[41] A. Kobialka, M. Sternik, and A. Ptok, Dynamical properties of the magnetic topological insulator TBi_2Te_4 (T = Mn, Fe): Phonons dispersion, Raman active modes, and chiral phonons study, Phys. Rev. B **105**, 214304 (2022).

[42] A. Kuhn, R. Chevalier, and A. Rimsky, Atomic structure of a 4*H* GaSe polytype named δ-type, Acta Crystallogr. B **31**, 2841 (1975).

[43] B. Schonfeld, J. J. Huang, and S. C. Moss, Anisotropic mean-square displacements (MSD) in single-crystals of 2*H*- and 3*R*-MoS_2, Acta Crystallogr. B **39**, 404 (1983).

[44] See Supplemental Material at http://link.aps.org/supplemental/10.1103/PhysRevB.106.184108 for two tables where atomic coordinates for the crystal structures of the magnetic topological insulators $MnBi_2Te_4$Å $\cdot\, n(Bi_2Te_3)$ with $n = \infty$, 1, 2, 4, and 5 (Table I) and $n = 0$, 3, and 6 (Table II) are provided.

[45] V. Chis, I. Yu. Sklyadneva, K. A. Kokh, V. A. Volodin, O. E. Tereshchenko, and E. V. Chulkov, Vibrations in binary and ternary topological insulators: First-principles calculations and Raman spectroscopy measurements, Phys. Rev. B **86**, 174304 (2012).

[46] Y. Zhao, X. Luo, J. Zhang, J. Wu, X. Bai, M. Wang, J. Jia, H. Peng, Z. Liu, S. Y. Quek, and Q. Xiong, Interlayer vibrational modes in few quintuple layer Bi_2Te_3 and Bi_2Se_3 two-dimensional crystals: Raman spectroscopy and first-principles studies, Phys. Rev. B **90**, 245428 (2014).

[47] M. Köpf, J. Ebad-Allah, S. H. Lee, Z. Q. Mao, and C. A. Kuntscher, Influence of magnetic ordering on the optical response of the antiferromagnetic topological insulator $MnBi_2Te_4$, Phys. Rev. B **102**, 165139 (2020).

[48] M. Köpf, S. H. Lee, H. Kumar, Z. Q. Mao, and C. A. Kuntscher, Infrared study of the layered, magnetic insulator $Mn(Bi_{0.07}Sb_{0.93})_2Te_4$ at low temperatures, Phys. Rev. B **105**, 195125 (2022).

[49] L. Ding, Ch. Hu, E. Feng, Ch. Jiang, I. A. Kibalin, A. Gukasov, M-F. Chi, N. Ni, and H. Cao, Neutron diffraction study of magnetism in van der Waals layered $MnBi_2nTe_{3n+1}$, J. Phys. D: Appl. Phys. **54**, 174003 (2021).